Doping-free Janus homojunction solar cell with efficiency exceeding 23%

View Online   Export Citation   CrossMark

Lei Li,[1] Zi-Xuan Yang,[1] Tao Huang,[1] Hui Wan,[1,2] Wu-Yu Chen,[1] Tao Zhang,[1] Gui-Fang Huang,[1,a] (ID) Wangyu Hu,[3] (ID) and Wei-Qing Huang[1,a] (ID)

AFFILIATIONS

[1] Department of Applied Physics, School of Physics and Electronics, Hunan University, Changsha 410082, China
[2] School of Materials and Environmental Engineering, Changsha University, Changsha 410082, China
[3] School of Materials Science and Engineering, Hunan University, Changsha 410082, China

[a] Authors to whom correspondence should be addressed: gfhuang@hnu.edu.cn and wqhuang@hnu.edu.cn

ABSTRACT

Photovoltaic solar cell is one of the main renewable energy sources, and its power conversion efficiency (PCE) is improved by employing doping or heterojunction to reduce the photogenerated carrier recombination. Here, we propose a straightforward strategy for constructing high-PCE homojunction solar cells, where intrinsic driving forces can simultaneously enhance the efficiency of carrier separation and transport. Thanks to the intrinsic dipole of Janus structure, doping-free Janus homojunction has naturally not only a type-II band alignment to promote the photoexciton dissociation, but also a reduced effective bandgap to enhance light absorption. More importantly, the interfacial dipole can facilitate the separation of carriers into different layers, thereby promoting carrier separation; and the intrinsic dipole across the Janus structure can drive photoinduced electron and hole transfer to opposite layers, enhancing carrier transport. We illustrate the concept in titanium-based Janus monolayer homojunction, where the theoretically observed PCE reaches 23.22% of TiSSe homojunction. In contrast to the previous cell architectures that require complex processing procedures and often result in defects, the doping-free homojunction configuration promises both high PCE and significantly lower manufacturing costs. Our work opens an avenue to design low-cost, high-efficiency solar cells.

Solar energy is the largest carbon-neutral energy source available today and the only fully renewable source that has the capability to meet the world's large and growing energy demand.[1–3] Photovoltaic solar cell, one of the most promising and efficient technologies to harvest this energy, can directly convert sunlight into electricity with zero operating carbon emissions.[4,5] The core of a typical solar cell consists of a photoactive layer (as light absorber) sandwiched by an electron-transport layer (ETL) and hole-transport layer (HTL) (Fig. 1).[6] The photoactive layer functions to convert photons into free charge carriers, while the ETL and HTL are crucial for separating and extracting these photogenerated carriers. Moreover, they block counter charge carriers and transport the charge carriers to the electrodes, resulting in photovoltage and photocurrent. Power conversion efficiency (PCE) is key for a solar cell,[7] which will determine whether it is competitive.

Both the materials and configurations of the photoactive layer lie at the heart of improving PCE. Various materials, including silicon,[6] compound semiconductors,[8,9] polymers,[10,11] organic dyes,[12] quantum dots,[13] and perovskites,[14,15] have been identified as suitable photoactive components for solar cells. Concurrently, to effectively separate the photogenerated carriers, several innovative configurations of the photoactive layer have been proposed. Single-junction configuration is used in a bulk heterojunction solar cell, as shown in Fig. 1(a).[11,16] However, the PCE of single-junction solar cell is still limited by non-ideal exciton dissociation and charge transport, because it is difficult to control the morphology of the phase separation into an interpenetrating network during the thin-film deposition process. Type-II heterojunction configuration can effectively separate the photogenerated carriers to different layers [Fig. 1(b)].[17–20] However, the conversion efficiency in such a bilayer heterojunction device is still limited: (1) Efficient charge separation occurs only at the interface, while the photo-excitations created far from the interface will recombine before diffusing to the interface; (2) even if charges are separated at the interface, the conversion efficiency is limited by the possible recombination of carriers during long distance transport before reaching transport layers. To reduce the carrier losses, a p–n homojunction structure is proposed [Fig. 1(c)], in which a doping-induced built-in electric field
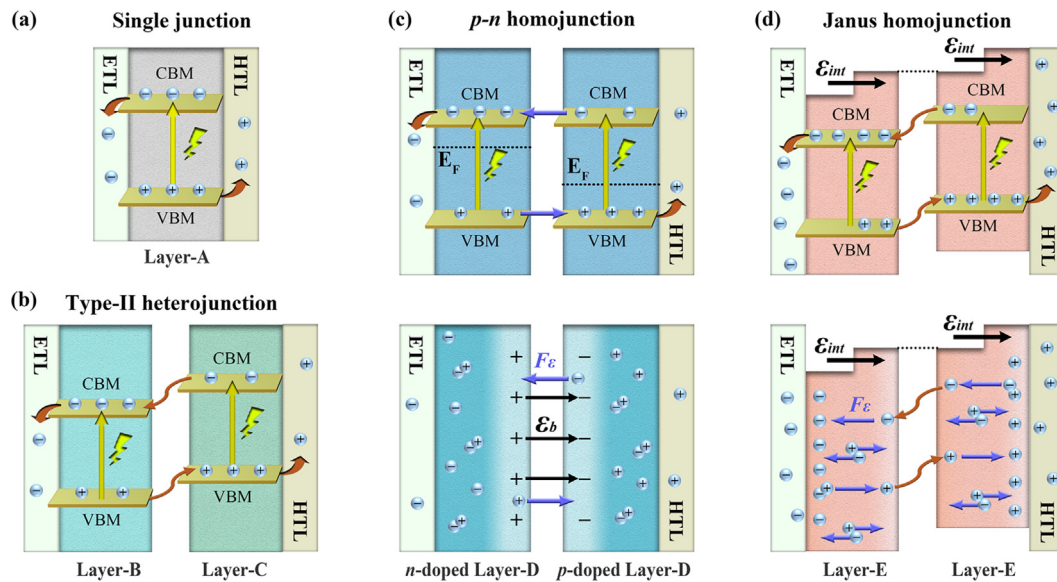
FIG. 1. The diagrams of solar cells based on (a) single junction, (b) type-II heterojunction, (c) p-n homojunction, and (d) Janus homojunction. There is no driving force for carrier migration, and the carriers are not separated in single junction (a); type-II heterojunction can separate the carriers to different monolayers, but there is still no driving force (b); the built-in electric field (ε_b) in p-n homojunction drives the carrier migration to different layers, but it can only appear in interlayer (c); the intrinsic electric field (ε_{int}) in Janus homojunction can drive the carrier migration to opposite directions in each Janus layer (d). The electric field force (F_ε) on the carrier is marked with blue arrows.

is formed that could enhance the oriented transport of the photo-induced electrons/holes.[21–23] To a certain degree, however, the doping homojunction structure has similar issues as in single junction and type-II heterojunction configurations. Even worse, the doped impurities will act as carrier recombination centers, thus increasing carrier losses. It naturally raises the question of whether there is a strategy to address these drawbacks.

Here, we demonstrate a doping-free Janus homojunction structure consisting of two-dimensional (2D) Janus semiconductors, as a photoactive component for solar cells, to achieve high PCE [Fig. 1(d)]. The intrinsic dipole induced by inversion symmetry-breaking[24] naturally results in a type-II band alignment in the Janus homojunction, facilitating the separation of photoexcitons at the interface. Additionally, the interfacial interaction leads to a reduced effective bandgap, enhancing light absorption. In particular, the intrinsic electric field in the Janus layer would drive the oriented transport of the photoinduced electrons and holes in opposite directions, thereby significantly reducing the carrier recombination losses. The results show that the Janus homojunction is an effective photoactive component, beyond existing heterojunction and doping homojunction, for solar cell to achieve high PCE with reduced carrier recombination losses by intrinsic properties.

To effectively separate photogenerated carriers, a type-II band alignment is generally adopted for exciton solar cells, as illustrated in Fig. 2(a). In such an alignment, the PCE can be derived as a function of the bandgap of the donor layer (E_g^d) and the conduction-band offset of the heterostructure (E_c), as shown in Fig. 2(b). Ideally, a solar cell can achieve a PCE exceeding 25% when E_g^d is near 1.5 eV and E_c approaches 0 eV. Customizing the band edges to fulfill these criteria is a complex task for a heterojunction or p–n homojunction. Here, we propose that constructing Janus homojunction by co-directional

stacking two Janus monolayers with their out-of-plane dipoles aligned in the same direction, as depicted in Fig. 2(c), is an effective strategy to remarkably simple this issue. Here, E_c is equal to electrostatic potential difference (ΔV), because the misalignment comes from the intrinsic dipole induced ΔV; E_g^d is equal to bandgap (E_g) of the monolayer, because two identical layers obviate the need to distinguish between donor and acceptor. Therefore, by utilizing a Janus monolayer with E_g of approximately 1.5 eV and ΔV approaching 0, we can effectively construct a homojunction that could realize high PCE.

To demonstrate our proposal, 2H-phase transition metal dichalcogenides (TMDs) monolayers are chosen as models due to their robust stability as semiconductor materials.[25–27] Their Janus counterparts MXY (where M represents center metal atom; $X, Y = $ O, Se, Se, Te; X is more electronegative than Y), not only inherit semiconductor properties but also introduce an additional intrinsic dipole.[28,29] The calculated dipole moments are illustrated in Fig. 2(d), with negative values indicating an abnormal direction. The positive direction of the dipole is defined as pointing from the side with lower electronegative atom (Y) to another side (X). It is observed that all Ti-based materials, as well as Zr- and Hf-based materials that lack oxygen, exhibit minimal dipole moments, with the majority displaying an anomalous direction. To explain the phenomenon, we simplify the dipole (μ) in three-atom-layer structure as two local dipoles (μ_X and μ_Y), which are from center metal to each side, as shown in Fig. 2(e), and the μ depends on the difference between them.[24] The μ_X and μ_Y are related to the charge transfer q_i and the distance d_i of the corresponding side,

$$\mu_i \sim q_i \cdot d_i; \quad (i = X, Y).$$

Because X is more electronegative than Y, it attracts more charge leading to larger q_X than q_Y, but simultaneously the X–M bond length is shorter than Y–M resulting in d_X to be less than d_Y, which creates a
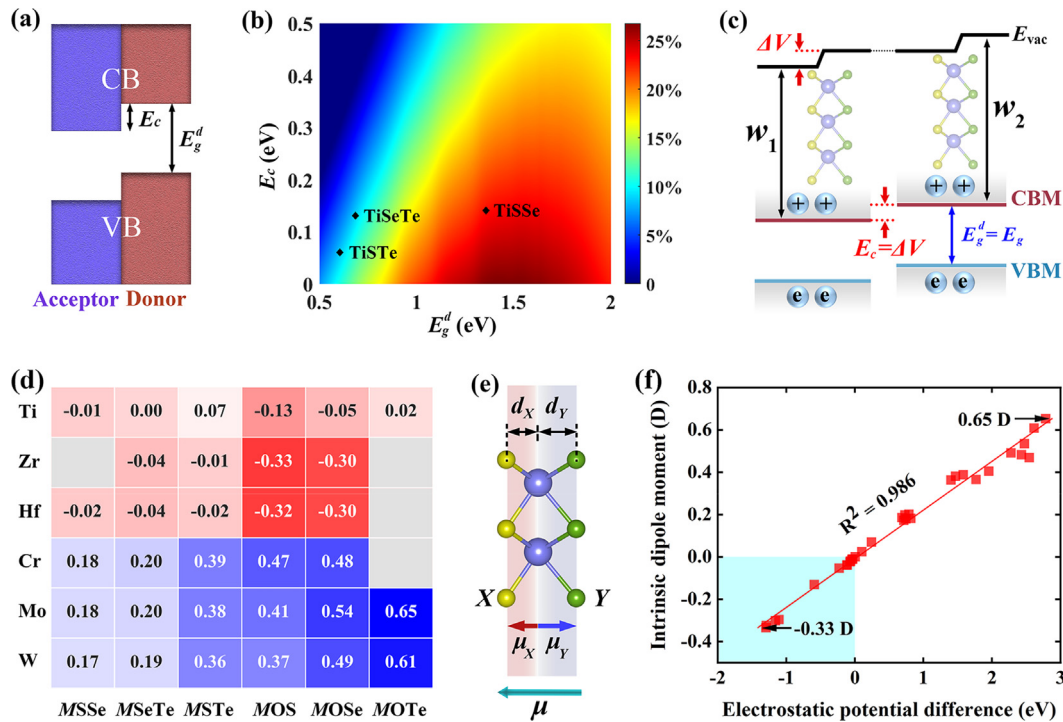
FIG. 2. (a) The type-II energy band alignment diagram. (b) Computed PCE contours as a function of the conduction band offset E_c and the donor bandgap E_g^d. (c) Band arrangement diagram of Janus homojunction. The (d) dipole moments, (e) dipole diagram, and (f) linear relationship between electrostatic potential differences and intrinsic dipole moments of 2H-phase Janus TMDs monolayers.

competitive relationship between μ_X and μ_Y. In the case μ_Y larger than μ_X, the direction of dipole would be anomalous, which is from X to Y atoms. As shown in Fig. S1, the linear relationship between intrinsic dipole moments and local dipole moments validates the feasibility of this simplified scheme, with the constant coefficient between them representing the similar level of electronic discretization in these three-atom-layer structures.

The intrinsic dipole acts like an effective electric field perpendicular to the monolayer plane,[30] inducing a ΔV on both sides. As shown in Fig. 2(f), there is a linear correlation between μ and ΔV. Here, to minimize E_c, TiXY (X, Y = S, Se, Te) monolayers that possess small dipoles are selected to construct homojunction, as displayed in Fig. 3(a), with their lattice constants listed in Table S1. For solar cell efficiency, the appropriate E_g is crucial. The energy band calculations reveal that all three structures are semiconductors, as illustrated in Fig. 3(b). Specifically, TiSSe possesses a moderate E_g of 1.59 eV, ideal for homojunction solar cells. However, TiSeTe and TiSTe possess E_g of 0.88 and 0.78 eV, respectively, which are too small for solar cells.

For comparative study, three TiXY monolayers are all used to construct homojunction. Here, five high-symmetry stacking styles denoted by AA, AA', $A'B$, AB', and AB are considered, as depicted in Fig. 3(c).[31,32] The layers are defined by the ligands on the respective vacuum side, termed layer-X and layer-Y. To find the most preferred stacking pattern, the energetic stability is assessed through the binding energy (E_b),

$$E_b = E_h - 2E_m,$$

where E_h and E_m are the DFT energies of corresponding homojunction and monolayer (Table S1), respectively. The $A'B$ stacking exhibits the highest E_b, and the energy differences relative to the $A'B$ stacking for other stacking are summarized in Fig. 3(d). The AA and $A'B$ stackings, with axially aligned ligands, experience interfacial repulsion, leading to higher E_b. In contrast, the AA', AB, and AB' stackings feature an axially staggered arrangement that fosters tighter structural bonding due to enhanced van der Waals interactions, especially for the AB' stacking, with the lowest E_b values of -7.26, -6.10, and -5.52 eV for TiSSe, TiSeTe, and TiSTe, respectively. The lattice constants (Table S1) show almost no difference compared to the corresponding monolayers. Consequently, the AB' stacking is chosen for the homojunction in this study. Figure 3(e) shows that there is a significant transfer of charge density from the layer-X to layer-Y under the AB' stacking, indicating strong interlayer charge transfer and stable bonding.

The photogenerated carrier separation is first tested. Figure 4(a) shows the density of states projected to two layers of the homojunctions. As expected, all homojunctions exhibit a type-II alignment, where the layer-Y contributing valence band maximum (VBM) acts as the donor and the layer-X contributing conduction band minimum (CBM) acts as the acceptor. The wave functions at VBM and CBM distributed in layer-Y and layer-X, respectively, as shown in Fig. 4(b), further confirm the effectively carrier separation capability. As a promising light absorber in solar cell, the ability of solar light harvesting is essential as well.[33] Thus, we examine the optical properties by calculating the absorption spectra for each monolayer and homojunction, as illustrated in Fig. 4(c). The homojunctions demonstrate
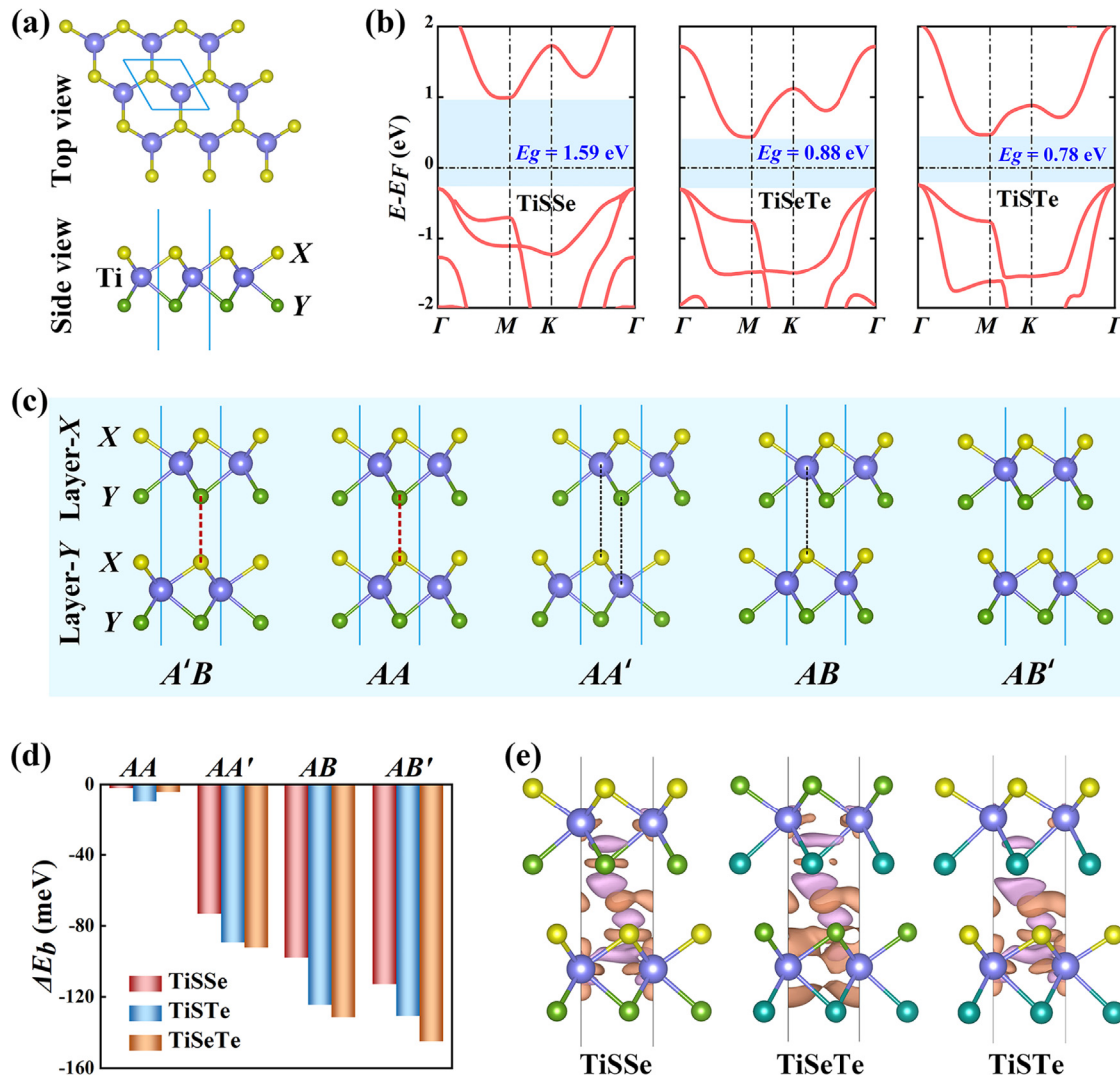
FIG. 3. The (a) top and side views and (b) energy bands of the TiXY monolayers. (c) Diagrams of the stacking styles of TiXY homojunction. (d) The binding energy differences to AB' stacking. (e) The charge density difference between two layers of TiXY homojunctions.

superior absorption in the visible-light region compared to their constituent monolayers, attributed to the reduced effective bandgap (E_g^e) upon homojunction formation and the reduced bandgap for both acceptor (E_g^a) and donor (E_g^d) as listed in Table I.

The approach that achieves a type-II band alignment and strong solar light harvesting capacity, is attributed to band bending induced by ΔV from the intrinsic dipole,[34] and the further reduced bandgap. In addition to the intrinsic dipole, there is an interlayer dipole in each homojunction due to charge transfer between two layers [Fig. 3(e)]. This interlayer dipole induces an additional interlayer electrostatic potential difference (ΔV_{int}), leading to a shift in the energy bands, as shown in Figs. 5(a)–5(c).

Unlike intrinsic dipoles, interlayer dipoles are solely associated with the charge transfer between the two ligand atoms at the interface. The direction is always from layer-X pointing toward layer-Y due to charge transfer occurring from the Y to X atoms of the interlayer. The intrinsic dipole direction, however, is not fixed and only aligns with the interlayer dipole direction under conditions of anomalous intrinsic dipole direction. In this case, E_c equals the sum of the individual electrostatic potential differences induced by both intrinsic and interlayer dipoles ($\Delta V + \Delta V_{int}$), as illustrated in the TiSSe homojunction depicted in Fig. 5(a). For TiSTe with a normal dipole direction, the intrinsic dipole and the interlayer dipole point in opposite directions. Consequently, E_c is determined by the difference between the electrostatic potential differences produced individually by two dipoles ($|\Delta V - \Delta V_{int}|$), as shown in Fig. 5(c). Since E_c in this case is a difference, it would obviously be smaller, which is beneficial to improve the PCE. For TiSeTe, where the intrinsic dipole is nearly zero, E_c is then solely contributed by ΔV_{int} [Fig. 5(b)].
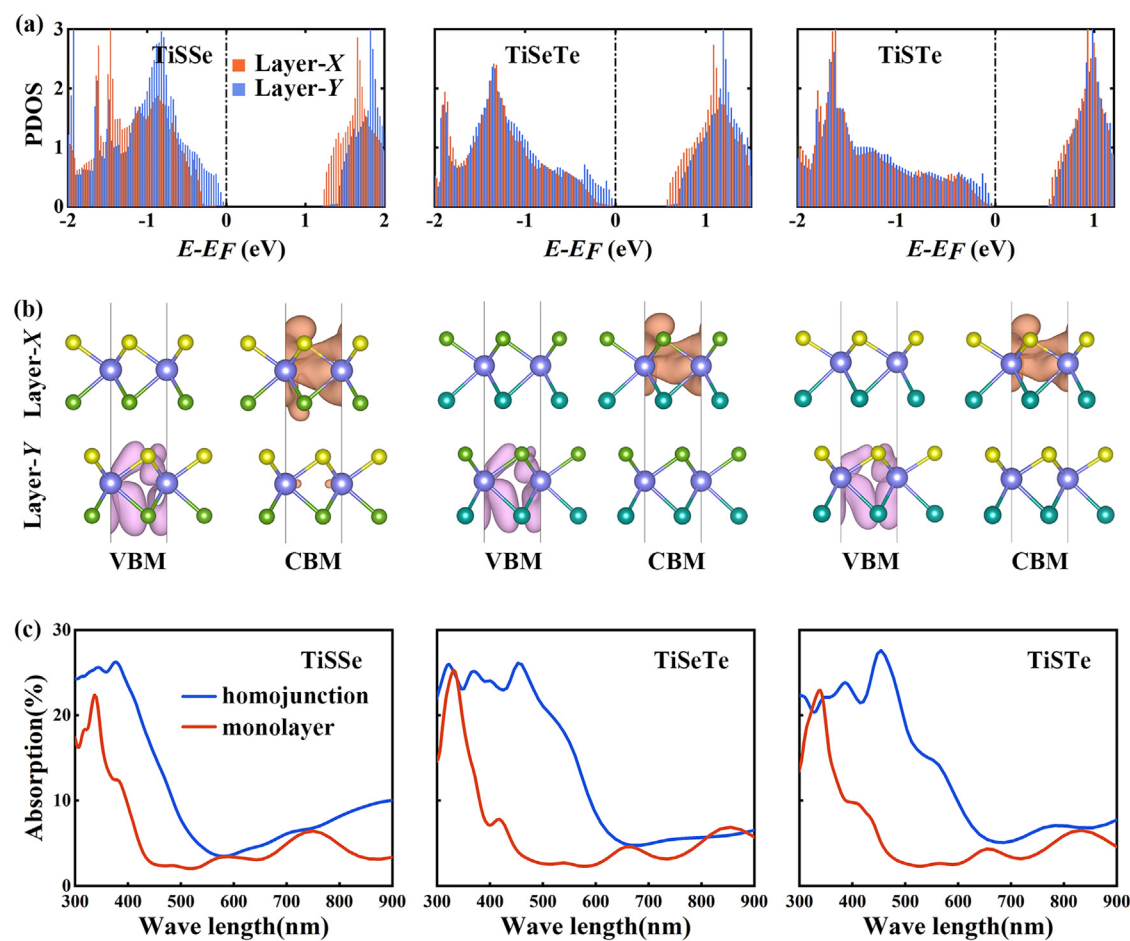
FIG. 4. The (a) density of states projected to two layers and (b) corresponding wavefunctions in CBM and VBM of TiXY homojunctions. (c) The absorption coefficients of TiXY monolayers and homojunctions.

The charge transfer not only induces an additional ΔV_{int} but also causes intralayer charge redistribution, which affects the intrinsic dipole of each layer and modifies E_g. Nonetheless, the former undergoes changes that are far less significant compared to the interlayer dipole, and the latter is influenced by more factors. For both two layers, interlayer dipole acts like an effective electric field applied to them, leading to a significant change in its bandgap due to the Stark

TABLE I. The bandgap E_g, electrostatic potential difference ΔV of TiSSe, TiSeTe, and TiSTe monolayers. The acceptor bandgap E_g^a, donor bandgap E_g^d, ratio of short circuit current density to AM1.5 solar energy flux J_{sc}/P_{solar} conduction band offset E_c, and PCE η of TiSSe, TiSeTe, and TiSTe homojunctions.

	Monolayer		Homojunction				
	E_g (eV)	ΔV (eV)	E_g^a (eV)	E_g^d (eV)	J_{sc}/P_{solar}	E_c (eV)	η(%)
TiSSe	1.58	−0.04	1.52	1.36	0.39	0.14	23.22
TiSeTe	0.88	0	0.77	0.69	0.54	0.13	9.08
TiSTe	0.78	0.24	0.66	0.61	0.54	0.06	8.86

effect.[35,36] As shown in Figs. 5(d)–5(f) and Table I, under the synergistic effects of charge redistribution and the Stark effect, both E_g^a and E_g^d of these homojunctions decrease. In fact, external electric fields can also induce the Stark effect in these materials. Here, we calculate the energy bands of TiSSe homojunction under external electric fields ranging from −0.3 to 0.3 V/Å, as depicted in Fig. S2. Due to the Stark effect, the bandgaps of both the acceptor and donor layers exhibit slight variations. Furthermore, as the electric field strength increases, the band edge positions of both the acceptor and donor layers show a linear change, as illustrated in Fig. S3. This linear response to the electric field is attributed to the vectorial superposition of the external electric field and the intrinsic field induced by the dipole, resulting in a linear influence on the band alignment. This indicates that we can utilize external electric fields to modulate the performance of Janus homojunction solar cells.

Based on E_c and E_g^d values, we can calculate ratio of short circuit current density to AM1.5 solar energy flux J_{sc}/P_{solar} and PCE η to measure the ability to convert photon energy into electric current, as listed in Table I. The calculated PCEs of TiSeTe and TiSTe homojunction are 9.08% and 8.86%, respectively, which are relatively low for
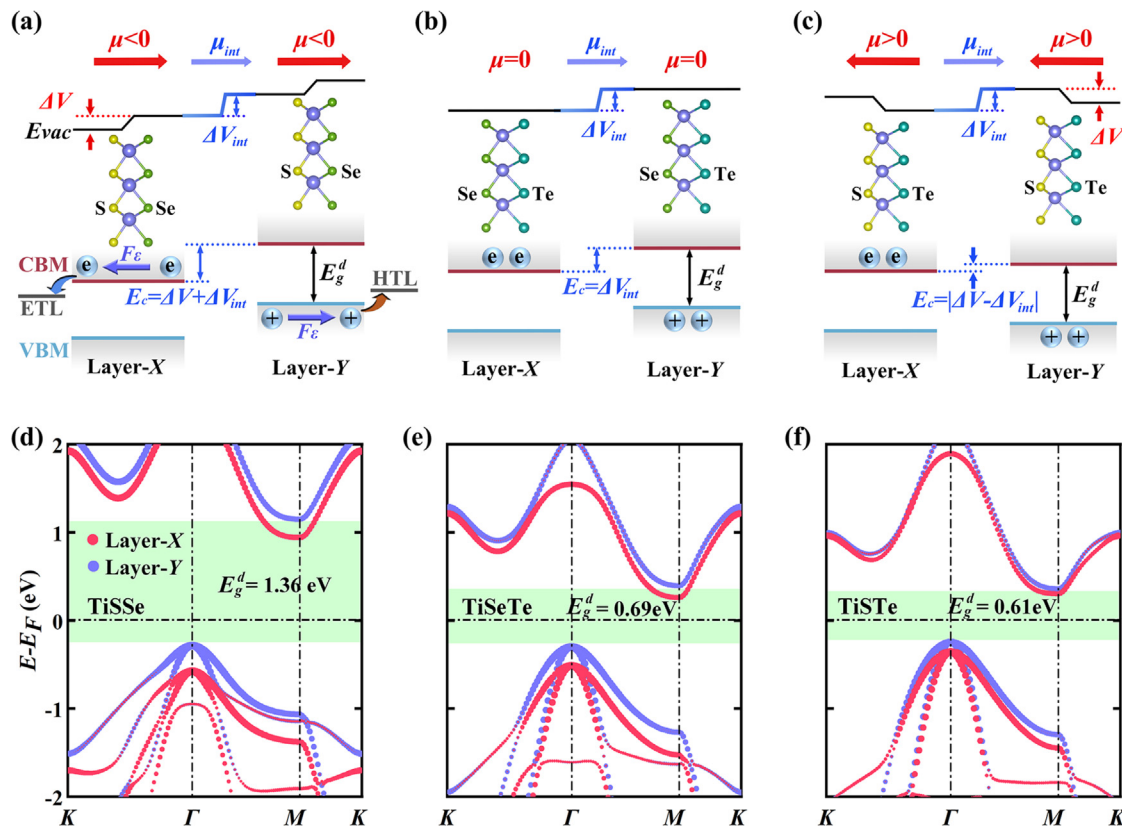
07 December 2024 07:55:41

FIG. 5. Band arrangement diagram of (a) TiSSe, (b) TiSeTe, and (c) TiSTe homojunctions. The energy bands projected to two layers of (d) TiSSe, (e) TiSeTe, and (f) TiSTe homojunctions.

applications. However, the TiSSe homojunction exhibits a significantly higher PCE up to 23.22%, which is much closer to the optimal efficiency target for solar cells and surpasses the PCE of many solar cells proposed based on the traditional strategy (Table S2). In particular, for the TiSSe case as shown in Fig. 5(a), the interlayer dipole induced interfacial electric field would drive carriers to separate into different layers; and the intrinsic electric field in the Janus layer would drive the oriented transport of the photoinduced electrons and holes to directions of ETL and HTL, respectively, promoting the carrier transfer to the electrode.

In summary, we propose a strategy to design high PCE solar cells with doping-free Janus homojunction based on 2D Janus semiconductors, exemplified by titanium-based monolayers like TiSSe. Consequently, our homojunctions inherently feature a type-II band alignment that enhances photoexciton dissociation, and a reduced effective bandgap that enhances light absorption, which can be attributed to the intrinsic dipole of the Janus monolayers. Moreover, the intrinsic dipole induced electric field can drive photoinduced electron and hole transfer from the interface to the opposite transport layers, respectively, further enhancing the efficiency of carrier separation and transport. We find that a minimal intrinsic dipole and an optimal bandgap are key to achieve high PCE. The TiSSe homojunction, in particular, achieves an impressive PCE of 23.22%, showcasing the potential of this strategy for developing solar cells that are both high-

performing and cost-effective. This work opens horizons for the creation of advanced solar cell materials with enhanced efficiency and simplified manufacturing processes.

See the supplementary material for the computational methods and additional results.

AUTHOR DECLARATIONS
Conflict of Interest

The authors have no conflicts to disclose.

Author Contributions

Lei Li: Data curation (lead); Formal analysis (lead); Investigation (lead); Methodology (lead); Writing – original draft (lead). **Zi-Xuan Yang:** Formal analysis (supporting); Investigation (supporting); Methodology (supporting). **Tao Huang:** Formal analysis (supporting); Investigation (supporting); Methodology (supporting). **Hui Wan:** Formal analysis (supporting); Investigation (supporting). **Wu-Yu**

Chen: Formal analysis (supporting); Investigation (supporting). **Tao Zhang:** Formal analysis (supporting); Investigation (supporting). **Gui-Fang Huang:** Investigation (lead); Methodology (lead); Writing – review & editing (lead). **Wangyu Hu:** Formal analysis (supporting); Methodology (supporting); Software (supporting). **Wei-Qing Huang:** Formal analysis (lead); Funding acquisition (lead); Investigation (lead); Methodology (lead); Writing – review & editing (lead).

DATA AVAILABILITY

The data that support the findings of this study are available within the article.

REFERENCES

[1] N. Guo, L. Yu, C. Shi, H. Yan, and M. Chen, "A facile and effective design for dynamic thermal management based on synchronous solar and thermal radiation regulation," Nano Lett. **24**, 1447–1453 (2024).

[2] P. Shi, J. Li, Y. Song, N. Xu, and J. Zhu, "Cogeneration of clean water and valuable energy/resources via interfacial solar evaporation," Nano Lett. **24**, 5673–5682 (2024).

[3] A. A. Ziabari and A. B. Khatibani, "Optical properties and thermal stability of solar selective absorbers based on Co–Al$_2$O$_3$ cermets," Chin. J. Phys. **55**, 876–885 (2017).

[4] L. Yan, J. Zhu, Q. Li, R. Ku, X. Huang, B.-T. Wang, H.-Z. Song, S. A. Yang, and L. Zhou, "Direct bandgaps, Weyl fermions, and strong light absorption ability in Janus Ti$_2$OFCl MOene," Appl. Phys. Lett. **122**, 043101 (2023).

[5] R. Stanton and D. J. Trivedi, "Charge carrier dynamics at the interface of 2D metal-organic frameworks and hybrid perovskites for solar energy harvesting," Nano Lett. **23**, 11932–11939 (2023).

[6] A. S. R. Bati, Y. L. Zhong, P. L. Burn, M. K. Nazeeruddin, P. E. Shaw, and M. Batmunkh, "Next-generation applications for integrated perovskite solar cells," Commun. Mater. **4**, 2 (2023).

[7] M. C. Scharber, D. Mühlbacher, M. Koppe, P. Denk, C. Waldauf, A. J. Heeger, and C. J. Brabec, "Design rules for donors in bulk-heterojunction solar cells—Towards 10 % energy-conversion efficiency," Adv. Mater. **18**, 789–794 (2006).

[8] Y. Gong, Q. Zhu, B. Li, S. Wang, B. Duan, L. Lou, C. Xiang, E. Jedlicka, R. Giridharagopal, Y. Zhou, Q. Dai, W. Yan, S. Chen, Q. Meng, and H. Xin, "Elemental de-mixing-induced epitaxial kesterite/CdS interface enabling 13%-efficiency kesterite solar cells," Nat. Energy **7**, 966–977 (2022).

[9] Y. Luo, G. Chen, S. Chen, N. Ahmad, M. Azam, Z. Zheng, Z. Su, M. Cathelinaud, H. Ma, Z. Chen, P. Fan, X. Zhang, and G. Liang, "Carrier transport enhancement mechanism in highly efficient antimony selenide thin-film solar cell," Adv. Funct. Mater. **33**, 2213941 (2023).

[10] H. Yu, Y. Wang, X. H. Zou, J. L. Yin, X. Y. Shi, Y. H. Li, H. Zhao, L. Y. Wang, H. M. Ng, B. S. Zou, X. H. Lu, K. S. Wong, W. Ma, Z. L. Zhu, H. Yan, and S. S. Chen, "Improved photovoltaic performance and robustness of all-polymer solar cells enabled by a polyfullerene guest acceptor," Nat. Commun. **14**, 2323 (2023).

[11] Z. C. He, B. Xiao, F. Liu, H. B. Wu, Y. L. Yang, S. Xiao, C. Wang, T. P. Russell, and Y. Cao, "Single-junction polymer solar cells with high efficiency and photovoltage," Nat. Photonics **9**, 174–179 (2015).

[12] A. Alizadeh, M. Roudgar-Amoli, S. M. Bonyad-Shekalgourabi, Z. Shariatinia, M. Mahmoudi, and F. Saadat, "Dye sensitized solar cells go beyond using perovskite and spinel inorganic materials: A review," Renewable Sustainable Energy Rev. **157**, 112047 (2022).

[13] L. Liu, A. Najar, K. Wang, M. Y. Du, and S. Z. Liu, "Perovskite quantum dots in solar cells," Adv. Sci. **9**, 2104577 (2022).

[14] Y. Y. Zhou, L. M. Herz, A. K. Y. Jen, and M. Saliba, "Advances and challenges in understanding the microscopic structure-property-performance relationship in perovskite solar cells," Nat. Energy **7**, 794–807 (2022).

[15] C. J. Tong, L. Li, L. M. Liu, and O. V. Prezhdo, "Synergy between ion migration and charge carrier recombination in metal-halide perovskites," J. Am. Chem. Soc. **142**, 3060–3068 (2020).

[16] K. Xiao, R. X. Lin, Q. L. Han, Y. Hou, Z. Y. Qin, H. T. Nguyen, J. Wen, M. Y. Wei, V. Yeddu, M. I. Saidaminov, Y. Gao, X. Luo, Y. R. Wang, H. Gao, C. F. Zhang, J. Xu, J. Zhu, E. H. Sargent, and H. R. Tan, "All-perovskite tandem solar cells with 24.2% certified efficiency and area over $1\,cm^2$ using surface-anchoring zwitterionic antioxidant," Nat. Energy **5**, 870–880 (2020).

[17] T. Huang, Z.-X. Yang, L. Li, H. Wan, T. Zhang, G.-F. Huang, W. Hu, and W.-Q. Huang, "Symmetry-breaking-enhanced power conversion efficiency of 2D van der Waals heterostructures," Appl. Phys. Lett. **125**, 033901 (2024).

[18] K. Liang, T. Huang, K. Yang, Y. Si, H.-Y. Wu, J.-C. Lian, W.-Q. Huang, W.-Y. Hu, and G.-F. Huang, "Dipole engineering of two-dimensional van der Waals heterostructures for enhanced power-conversion efficiency: The case of Janus Ga$_2$SeTe/InS," Phys. Rev. Appl. **16**, 054043 (2021).

[19] Y. Si, H.-Y. Wu, K. Yang, J.-C. Lian, T. Huang, W.-Q. Huang, W.-Y. Hu, and G.-F. Huang, "High-throughput computational design for 2D van der Waals functional heterostructures: Fragility of Anderson's rule and beyond," Appl. Phys. Lett. **119**, 043102 (2021).

[20] V. G. Garcia, N. N. Batista, D. A. Aldave, R. B. Capaz, J. J. Palacios, M. G. Menezes, and W. S. Paz, "Unlocking the potential of nanoribbon-based Sb$_2$S$_3$/Sb$_2$Se$_3$ van-der-Waals heterostructure for solar-energy-conversion and optoelectronics applications," ACS Appl. Mater. Interfaces **15**, 54786–54796 (2023).

[21] P. Calado and P. R. F. Barnes, "Ionic screening in perovskite p–n homojunctions," Nat. Energy **6**, 589–591 (2021).

[22] P. Cui, D. Wei, J. Ji, H. Huang, E. Jia, S. Dou, T. Wang, W. Wang, and M. Li, "Planar p–n homojunction perovskite solar cells with efficiency exceeding 21.3%," Nat. Energy **4**, 150–159 (2019).

[23] Z. Zhao, M. Sun, Y. Ji, K. Mao, Z. Huang, C. Yuan, Y. Yang, H. Ding, Y. Yang, Y. Li, W. Chen, J. Zhu, J. Wei, J. Xu, W. Paritmongkol, A. Abate, Z. Xiao, L. He, and Q. Hu, "Efficient homojunction tin perovskite solar cells enabled by gradient germanium doping," Nano Lett. **24**, 5513–5520 (2024).

[24] L. Li, T. Huang, K. Liang, Y. Si, J. C. Lian, W. Q. Huang, W. Y. Hu, and G. F. Huang, "Symmetry-breaking-induced multifunctionalities of two-dimensional chromium-based materials for nanoelectronics and clean energy conversion," Phys. Rev. Appl. **18**, 014013 (2022).

[25] X. Sui, T. Hu, J. Wang, B.-L. Gu, W. Duan, and M-s Miao, "Voltage-controllable colossal magnetocrystalline anisotropy in single-layer transition metal dichalcogenides," Phys. Rev. B **96**, 041410 (2017).

[26] F. A. Rasmussen and K. S. Thygesen, "Computational 2D materials database: Electronic structure of transition-metal dichalcogenides and oxides," J. Phys. Chem. C **119**, 13169–13183 (2015).

[27] C. Ataca, H. Şahin, and S. Ciraci, "Stable, single-layer MX$_2$ transition-metal oxides and dichalcogenides in a honeycomb-like structure," J. Phys. Chem. C **116**, 8983–8999 (2012).

[28] L. Dong, J. Lou, and V. B. Shenoy, "Large in-plane and vertical piezoelectricity in Janus transition metal dichalchogenides," ACS Nano **11**, 8242–8248 (2017).

[29] C. Zhang, Y. Nie, S. Sanvito, and A. Du, "First-principles prediction of a room-temperature ferromagnetic Janus VSSe monolayer with piezoelectricity, ferroelasticity, and large valley polarization," Nano Lett. **19**, 1366–1370 (2019).

[30] A. Strasser, H. Wang, and X. F. Qian, "Nonlinear optical and photocurrent responses in Janus MoSSe monolayer and MoS$_2$-MoSSe van der Waals heterostructure," Nano Lett. **22**, 4145–4152 (2022).

[31] G. Constantinescu, A. Kuc, and T. Heine, "Stacking in bulk and bilayer hexagonal boron nitride," Phys. Rev. Lett. **111**, 4145–4152 (2013).

[32] W. Zhou, J. Chen, Z. Yang, J. Liu, and F. Ouyang, "Geometry and electronic structure of monolayer, bilayer, and multilayer Janus WSSe," Phys. Rev. B **99**, 075160 (2019).

[33] M. Mirzaei, J. Hasanzadeh, and A. A. Ziabari, "Efficiency enhancement of CZTS solar cells using Al plasmonic nanoparticles: The effect of size and period of nanoparticles," J. Electron. Mater. **49**, 7168–7178 (2020).

[34] Y. Gao, Q. Zhang, W. Hu, and J. Yang, "First-principles computational screening of two-dimensional polar materials for photocatalytic water splitting," ACS Nano **18**, 19381–19390 (2024).

[35] A. Ramasubramaniam and D. Naveh, "Piezoelectric electrostatic superlattices in monolayer MoS$_2$," Phys. Rev. Mater. **8**, 014002 (2024).

[36] A. Bera, A. Maiti, and A. J. Pal, "Emergence of a hidden topological insulator phase in hybrid halide perovskites," Appl. Phys. Lett. **123**, 133103 (2023).